

**This item is the archived peer-reviewed author-version of:**

Wet-STEM tomography : principles, potentialities and limitations

**Reference:**

Masenelli-Varlot Karine, Malchere Annie, Ferreira Jose, Heidari Mezerji Hamed, Bals Sara, Messaoudi Cedric, Garrido Sergio Marco.- *Wet-STEM tomography : principles, potentialities and limitations*

**Microscopy and microanalysis** - ISSN 1431-9276 - 20:2(2014), p. 366-375

DOI: <http://dx.doi.org/doi:10.1017/S1431927614000105>

Handle: <http://hdl.handle.net/10067/1184110151162165141>

# **Wet-STEM tomography: principles, potentialities and limitations**

K. Masenelli-Varlot<sup>1\*</sup>, A. Malchère<sup>1</sup>, J. Ferreira<sup>1</sup>, H. Heidari Mezerji<sup>2</sup>, S. Bals<sup>2</sup>, C. Messaoudi<sup>3,4</sup>, S. Marco<sup>3,4</sup>

<sup>1</sup>Université de Lyon, INSA-Lyon, MATEIS UMR5510, 7 avenue J. Capelle, 69621 Villeurbanne cedex, France.

<sup>2</sup>EMAT, University of Antwerp, Groenenborgerlaan 171, B-2020 Antwerp, Belgium

<sup>3</sup>Institut Curie, Centre de Recherche, Centre Universitaire d'Orsay, Bât. 112., 91405 Orsay cedex, France

<sup>4</sup>INSERM U759, Centre Universitaire d'Orsay, Bât. 112, 91405 Orsay cedex, France

\*Corresponding author: Karine.Masenelli-Varlot@insa-lyon.fr ; phone +33 (0) 472 437 103; fax +33 (0) 472 437 930.

## **Abstract**

The characterization of biological and inorganic materials by determining their 3D structure in conditions closer to their native state is a major challenge of technological research. Environmental scanning electron microscopy (ESEM) provides access to the observation of hydrated samples in water environments. Here, we present a specific device for ESEM in the Scanning Transmission Electron Microscopy (STEM) mode, allowing the acquisition of tilt-series suitable for tomographic reconstructions. The resolution which can be obtained with this device is first determined. Then, we demonstrate the feasibility of tomography on wet materials. The example studied here is hydrophilic mesoporous silica (MCM-41). Finally, the minimum thickness of water which can be detected is calculated from Monte Carlo simulations and compared to the resolution expected in the tomograms.

Keywords : Wet-stem, Tomography, Environmental, Monte Carlo simulation

## **Introduction**

Tomography has become a key characterization tool in materials science as well as in biology. The principle of tomography is based on the acquisition of a series of projection images at different tilt angles, and on the calculation of the 3D reconstructed volume (tomogram) using dedicated algorithms. Several tomography techniques are available, using different types of radiations, depending on the observation scale. X-rays are currently used for the 0.5  $\mu\text{m}$ –1 mm resolution level (Maire et al., 2001) and the three-dimensional characterization of nanoscaled structures requires transmission electron microscopy (TEM) tomography (Koster et al. 2000) or an atom-probe approach (Blavette et al. 1993). At the mesoscopic scale, corresponding to a resolution level between 10 nm and 500 nm, Scanning Electron Microscopy (SEM)-based techniques – such as Focused ion Beam (FIB) (Kubis et al., 2004) or serial block face SEM (Mancuso, 2012) – use a slice-and-view method to directly obtain slices of the materials volume. It has also been proposed to perform electron tomography in the Environmental SEM (ESEM), with a STEM detector placed under the tilted sample (Jornsano et al. 2011). At this stage, one can mention the specificity of ESEM, for which a partial pressure of gas is introduced in the sample chamber (Nelson, 1988). Whereas the gas molecules amplify the signal for secondary electron detection (Fletcher et al., 1997), they are used only to neutralize the excess charges when using a STEM detector. However, it has been shown that using water as environment, with a partial pressure around 5 Torr, and maintaining the sample temperature to 2 °C, it was possible to observe wet samples inside the ESEM (Donald, 2003).

The observation of wet samples requires dedicated specimen holders or microscopes, either in TEM or SEM. Whereas the first system in TEM was composed of an open environmental chamber (Ruska, 1942), it seems that the use of sealed liquid cells has become

predominant for TEM observations, since it allows a good stability - no evaporation or condensation - and controlled thickness of the water film (de Jonge & Ross, 2011). STEM-in-TEM observations on sealed cells have for instance allowed the observation of live eukaryotic cells (Peckys & de Jonge, 2011) and the investigation of the movement of nanoparticles in liquid (Ring & de Jonge, 2012). Yet, tilting the sample to perform tomographic acquisition would probably be hindered by the geometry of the sealed cell. Indeed, at increasing tilt angles, the electrons will have to pass through an increasing thickness of SiN (walls of the sealed cell) in addition to the increasing thickness of the water film. The thick support, surrounding the electron transparent window, may also hide the region of interest when tilting the sealed cell. In ESEM, the presence of the gaseous environment and the control of the sample temperature have also permitted the imaging of nanoparticles in liquid with a nanometer resolution, through STEM-in-SEM observations (Bogner et al., 2005). Because of the absence of a sealed cell, the thickness of the water film remains unknown and variations can lead to contrast inversions (Bogner, 2006). On the contrary, its main advantage lays in the fact that water condensation or evaporation can be tuned by varying the environmental pressure, which enables in situ hydration / dehydration experiments.

In this paper, we describe the development of a new device for electron tomography in the ESEM, which enables the acquisition of image series on wet samples. After a brief description of the device, the best achievable resolution will be determined on dry volumes. Then, the specificities of a 3D characterization of hydrated samples will be discussed. In particular, the influence of the size and the stability of water on parameters such as the number of projections or the choice of the reconstruction algorithm will be discussed. Finally, Monte Carlo simulations will be used to estimate the minimum quantity of water which can be detected.

## Materials and Methods

The wet-STEM tomography device, shown in Figure 1, has been designed according to the literature (Gauthier et al., 2006) (Jornsano et al., 2011). The device comprises three main parts: a) a tilting system ensured by a rotating piezoelectric system, b) a two-translation piezoelectric system to position the area of interest at the eucentric position and keep it in the field of view while tilting, c) a sample holder, which can be either a cylindrical tip or tweezers, and d) a detection system. A Peltier stage, not shown in Figure 1 but schematically represented by a dashed rectangle, is placed vertically between the piezoelectric elements and the sample. The cold transfer by conduction is ensured from the Peltier stage to the sample holder by slight friction. A thermocouple is inserted in the Peltier stage. The sample temperature is then controlled through the controller of the FEI conventional Peltier stage.

The wet-STEM tomographic device is placed in a XL-30 FEG ESEM from FEI, operating at 30 kV. The probe current was estimated to be equal to 240 nA for a 8 nm probe size (spot size 3). A Gaseous Secondary Electron Detector (GSED) was placed to perform the first observations, then a Backscattered Electron detector placed under the sample (as shown in Figure 1 – part d) detection system) was used for the STEM observations. As the presence of gas in the specimen chamber results in a broadening of the incident electron beam, known as the skirt effect, a Pressure Limiting Aperture cone was placed on the objective lens to reduce the loss of resolution due to the skirt effect by decreasing the distance the incident electrons have to travel along in the gaseous environment (Danilatos, 1993).

A 1  $\mu$ l of aqueous suspension of gold/polysiloxane nanoparticles (Martini et al. 2010) has been directly deposited onto a copper 300-mesh TEM grid covered with a holey carbon film. The pumping step, as well as the sample temperature and water pressure were optimized to prevent evaporation of the suspension droplet in the microscope. Then, the water pressure was decreased until the droplet was thin enough to get STEM images. Powders of Mobil

Crystalline Materials (MCM-41; Trewyn et al., 2007) have been directly – i.e. without any embedding or conductive coating - deposited on a copper 300-mesh TEM grid covered with a holey carbon film. At the beginning of the experiment, the MCM-41 grains were in the dry state. Then, the water pressure was slowly increased so that water condensed onto the MCM-41 grains and the holey carbon film. Each time, the working distance was set to 11 mm and the sample-to-detector distance was chosen to be 10 mm. With such a configuration, the electrons collected are those which have been scattered by the sample with angles ranging between 14 and 40°. 1290 x 968 images have been acquired in the STEM mode at different tilts, the tilt angles being set with an accuracy of 1 m°. The projection series have been aligned using Gatan<sup>TM</sup> Digital Micrograph and/or TomoJ (Messaoudi et al., 2007). Reconstructions have been calculated using standard algorithms, after denoising with the BgART algorithm (Messaoudi et al., 2013), or using Total Variation Minimisation (Goris et al., 2012). Fourier Shell Correlation (FSC) analysis (Harauz & Van Heel, 1986) has been performed using the software downloadable free of charge from the Image Science web site ([www.ImageScience.de](http://www.ImageScience.de)). Two reconstructed volumes are calculated from the tilted series, one with odd images and the other one with even series. Then, the FSC algorithm compares the two volumes by measuring the normalized cross-correlation coefficient over corresponding shells of constant spatial frequencies. The spatial frequency corresponding to the intersection of the FSC curve and a previously defined criterion indicates the resolution on the volumes. Then, the resolution on the full tomogram is estimated to be equal to half the resolution determined on the even/odd volumes.

Monte Carlo simulations have been performed with the software Hurricane® from SAMx. A scheme of the geometry chosen is displayed in Figure 2. MCM-41 was modeled by pure silica (SiO<sub>2</sub>) with a density of 0.9 g.cm<sup>-3</sup>. The lateral dimensions of the MCM-41 film have been chosen to be equal to 5 µm to reduce the fraction of electrons escaping the sample

through the lateral surfaces. The holey carbon film covering the copper grid was considered to be thin enough and has been neglected in the simulations. Moreover, as the MCM-41 grains are hydrophilic, it will be assumed that water preferentially condenses onto MCM-41 and not onto the carbon film. As a consequence, a single homogeneous water layer ( $\text{H}_2\text{O}$ , density  $1 \text{ g.cm}^{-3}$ ) is placed on the top of the MCM-41 film. The paths of 100,000 electrons have been calculated. The collection angles were chosen to range between  $14$  and  $40^\circ$ , in accordance with the experimental geometry. Thus, the number of collected electrons will refer to the number of electrons which have passed through the water-MCM-41 computation box and which have been scattered with angles ranging between  $14$  and  $40^\circ$ .

## **Results and discussion**

### *Best achievable resolution*

Figure 3a displays an image of gold/polysiloxane nanoparticles. Such nanoparticles exhibit a gold core of about  $5 \text{ nm}$  (Martini et al., 2010), which will be used to probe the resolution of the tomographic device. A typical image obtained in bright field Transmission Electron Microscopy (TEM) is shown in Figure 3b. Initially in suspension in water, their morphology is not greatly affected by water evaporation. In this section, we will thus probe the intrinsic resolution of STEM in SEM coupled with the mechanical stability of the tomographic device.

As the STEM detector collects scattered transmitted electrons, the gold core appears brighter than the polysiloxane shell. The gold core diameter is measured to be equal to  $8 \text{ nm}$ , which is the diameter of the probe size used for the observations. Care was taken during the pumping procedure to keep the water pressure well above the dew point. Moreover, during the first observations, the water pressure was slowly decreased from  $8 \text{ Torr}$  to  $5.6 \text{ Torr}$ , to reach a steady state. Despite this strict protocol, the thickness of the water film cannot be

measured and because of high surface tensions, the nanoparticles may be in the dry state. Nevertheless, the nanoparticle gold core will be a good probe of the resolution which can be obtained at best with our tomographic device.

The tomogram, calculated with a SIRT algorithm from a projection series of 41 images, with a tilt step of  $2^\circ$  (tilt range  $\pm 40^\circ$ ), is presented in Figure 3c. For a better clarity, the gold cores have been segmented and are highlighted in red on the tomogram displayed in Figure 3c. The polysiloxane shells seem quite flat, which is undoubtedly an artifact of irradiation damage. Indeed, it has been shown polysiloxane molecules undergo crosslinking (Si-O-Si chains) under irradiation. This has previously been shown to induce a collapse of the pores in open cell foams (Huang et al., 2002). When comparing the images at tilt angle of zero before and after the acquisition of half the tilt series, the polysiloxane shells have indeed spread out. Nevertheless, this did not affect the position of the gold cores, which have been successfully reconstructed.

The resolution in the tomogram has been determined by FSC (Harauz & Van Heel, 1986) by comparing the tomograms calculated from even and odd projections, see Figure 3d. The criterion chosen is 0.5 since the other criterions ( $\sigma$ , half-bit) cannot apply in this case by lack of intersection. With the 0.5 criterion, the FSC resolution in the full tomogram is estimated to be equal to 1 nm. However, it has to be mentioned that the curve does not yield a meaningful result since it does not drop to zero at high frequencies, most probably because of vibrations arising from water vibrations in the Peltier stage, leading to a horizontal noise in the images. Nevertheless, the 0.5-FSC resolution is close to the pixel size (0.9 nm) but is actually less than the experimental probe size (8 nm) and thus has no physical meaning. As a consequence, it is concluded that the resolution is not limited by the wet-stem tomography device capabilities but by the experimental conditions such as the probe size.

### *Specificities of the acquisition of tilt series on samples containing water*

Figure 4 displays raw images of MCM41, a silica mesoporous material at two different hydration states. MCM41 is an electron-resistant material. Due to its hydrophilic behavior, water will preferentially condense onto MCM41 rather than onto the carbon film. This experiment will therefore be used to prove the concept of wet-STEM tomography, i.e. tomography on wet materials.

The observation scale, chosen as a function of the grain size, does not permit the observation of the pore arrangement in the MCM41 grains. Indeed, with this magnification, 1 pixel represents 13 nm whereas the pore diameter is in the 5 nm range. In the wet state, a droplet of water has condensed close to the MCM-41 grain, see on the top of Figure 4e. Moreover, when comparing Figure 3b and 3e, the smallest features on the wet MCM-41 grain seem to be blurred, and the contour of the grain is broadened. The disappearance of small features is clearly visible in Figure 4g, which represents the variations of the grey level along a line in the images at tilt equal to  $0^\circ$  (Figure 4b and 4e). The water pressure increase cannot lead to such a loss of resolution, since the skirt effect is limited by the use of a cone on the gaseous secondary electron detector located at the bottom of the objective lens. The changes between the dry and wet states are attributed to the presence of water, as expected from the hydrophilic behavior of MCM-41. Collapses of the pore structure of MCM41 have previously been shown to occur when exposed to liquid water (Zhao et al. 1998) or even water vapor (Ribeiro Carrott et al., 1999). In our case, on the basis of images before and after the acquisition or the tilt series, it will be assumed, at our observation scale, that the morphology of the MCM41 grain is not altered by water.

Attempts have been made to investigate the stability – in size and shape - of the water droplet during tilting. Whereas the droplet shape seems to be rather stable, irradiation damage and/or temperature instabilities induce undesirable evaporation of the water droplet (not

displayed). The electron dose received by the sample was thus reduced by using a low-dose-like acquisition: the focus was set outside the region of interest, which was irradiated only during the acquisition of the tilt series. With an acquisition time of 3.36 ms per line, corresponding to 3.25 seconds per image, the number of projection series had to be reduced to 13 to minimize the water evaporation. Taking into account a pixel size of 13 nm, this corresponds to a dose received equal to  $48 \text{ C.m}^{-2}$  – or  $300 \text{ e}^{-}/\text{nm}^2$  - after the acquisition of the last image. Moreover, in order to reduce artifacts in the tomogram (Weyland, 2002), the tilt range has been kept as large as possible ( $\pm 50^\circ$ ), while the tilt step has been increased up to  $10^\circ$ . Despite such acquisition conditions, it can be seen on the top of Figure 5d (the last image of the tilt series) that the water droplet has partially evaporated. Nevertheless, the tilt series was kept for tomographic reconstructions. Indeed, the hydrophilic behavior of MCM-41 makes the evaporation of water from the MCM-41 grain more difficult than the evaporation of water from the carbon film. It will thus be assumed that the MCM-41 is still in the wet state.

The tomogram of wet MCM-41, calculated with conventional algorithms, contains a lot of artifacts, as expected due to the large tilt step. Denoising algorithms such as BgART have been found to improve the reconstructed volume (Messaoudi et al., 2013). BgART is an iterative reconstruction algorithm that removes the noise, considered as Gaussian white, in the background preserving the object signal. The reconstruction at step  $n$  is thresholded using  $\text{mean} + k * \text{sigma}$ , where mean and sigma are the average voxel value and standard deviation of the reconstruction respectively, and  $k$  a user-defined factor describing the level of noise. Values below threshold are put to mean value and values above threshold are kept identical. An iteration of the reconstruction process is then applied. At the end, the background is uniform while the object keeps its intensity values. Figure 5 displays the tomogram obtained with the ART algorithm after BgART denoising. Unfortunately, the improvement of the

signal-to-noise ratio does not compensate the fact that the tilt step is too large, as the XZ slice still contains a lot of artifacts.

Algorithms such as Compressed Sensing (Leary et al., 2012) or Total Variation Minimization (TVM) (Goris et al., 2012) (Goris et al., 2013) have shown to give more reliable tomograms from tilt series containing a limited number of projections. These algorithms are real-space iterative reconstruction techniques which assume that the object to be reconstructed has a sparse variation, meaning that only sharp gray value transitions in the reconstructed object are allowed. The TVM algorithm, used below, attempts to find a solution to the reconstruction problem by minimizing the total variation. A way to implement this constraint is by minimizing the norm of discrete gradient (i.e. total variation) of the reconstructed image and minimizing the projection distance simultaneously between the reconstructed object and original projections. Figure 6 shows the tomogram obtained by TVM. The overall shape of the MCM-41 grain, as well as the water droplet and the small features at the bottom of the MCM-41 grain in Figure 4e are resolved in the tomogram. The resolution in the tomogram may not be determined from FSC, because odd and even tilt series would contain very few images. Nevertheless, the smallest features in the tomogram are about 40 nm, which indicates that the resolution is at least equal to 40 nm.

#### *Numerical determination of the minimum water layer thickness*

In this section, we discuss the results of Monte Carlo simulations on a computation box containing a thin film of MCM-41 of varying thickness, eventually covered by a layer of water, also of varying thickness. Figure 7a displays the number of collected electrons as a function of the MCM-41 thickness. The curves for different water layer thicknesses all have the same overall shape, with a maximum when the MCM-41 thickness is equal to 2  $\mu\text{m}$ . For MCM-41 grains thinner than 1  $\mu\text{m}$ , the number of electrons increases since an increase of the

sample thickness leads to an increase of the number of scattering events and thus of the scattering angles. On the contrary for MCM-41 grains thicker than 2  $\mu\text{m}$ , the increase of the number of scattering events still leads to an increase of the scattering angles, which will exceed the maximum collection angle. Interestingly, at small MCM-41 thicknesses (below 1  $\mu\text{m}$ ), a slight shift of the curves is observed, see Figure 7b, which is the result of the increasing thicknesses – MCM-41 and water - the electrons have to pass through.

Based on the variations of the number of collected electrons, and considering that during the experiments, the detector brightness and contrast are adjusted on the dry state and remain unchanged during water condensation, a contrast can be defined as  $\frac{|n_{dry}-n_{wet}|}{n_{dry}}$  where  $n_{wet}$  and  $n_{dry}$  are the numbers of collected electrons with and without water, respectively. The variations of the contrast are shown in Figure 8. When arbitrarily setting a contrast detection limit greater than or equal to 5% maximum MCM-41 thickness can be defined for each water layer thickness. The values are summarized in Table 1.

Similar studies have been performed to determine the maximum sample thickness required to detect layers of water of 10, 20, 30 and 50 nm thick. The materials which were included in the simulations were SBA-15 (another mesoporous silica), carbon, dense silica, calcium carbonate, titanium oxide and alumina. The results are presented in Table 1. Linear regressions have been investigated between the sample and the water thickness. The coefficients of determination greatly differ from one material to the other. Using a F-test for regression, it is possible to state whether the coefficients of determination are significantly different from 0 or not. In such a test, the critical value of the F distribution is equal to 18.5 when considering 4 points, and a level of significance of 95%, which corresponds to a critical determination coefficient of 0.9025. It can therefore be concluded that the coefficients of determination are significantly larger than zero for MCM-41, pure silica and titanium oxide,

only. When investigating linear relationships between the sample thicknesses and densities, for fixed water thicknesses and with a significance level of 95%, the coefficients of determination are far lower than the critical value, 0.5692. It is thus concluded that for a given water thickness, the maximum sample thickness enabling the detection of this water film thickness does not depend on sample density. This conclusion is confirmed by another statistical test, an analysis of variance of the sample thickness, with two factors - the sample density and the water thickness. With a level of confidence of 95%, it is found that the maximum sample thickness depends on the water thickness but not on the sample density.

Since the maximum sample thickness which permits detection of a given thickness of water does not depend on the sample density, the average sample thickness has been calculated for each water thickness, see Table 1. For each average sample thickness, it is possible to estimate the resolution which can be obtained during a tomography experiment. The Crowther's criterion states that the lateral resolution  $d$  will be equal to  $\pi D/N$ , where  $D$  is the sample thickness and  $N$  the number of projections (Crowther et al., 1970). According to the Crowther's criterion, the resolutions in the tomograms have been estimated for each water thickness with sample thicknesses equal to the previously determined average sample thicknesses (see Table 1) and tilt steps of  $10^\circ$ . Interestingly, for one sample thickness, the values found from the Crowther's criterion are of the same orders of magnitude as the minimum water thicknesses. The slight differences observed could easily be explained by the fact that the Crowther's criterion considers the resolution in 3D, whereas the sample thicknesses have been determined from Monte Carlo simulations in 2D. In conclusion, it is expected from Monte Carlo simulations that the thickness of the water film which can be detected during wet-STEM tomography experiments will not significantly depend on the sample density but will rather be determined from the tomography experimental conditions (sample thickness, tilt step).

## Conclusions

We have demonstrated in this work the feasibility of tomography on wet samples observed using environmental scanning electron microscopes (ESEM) by using a dedicated device. Mechanical vibrations and tilt positioning do not limit the resolution in the tomogram. Indeed, it has to be measured equal to a few nm on gold/polysiloxane core-shell nanoparticles – most probably in the dry state. Tilt series of MCM41 grains in the wet state have been acquired and the experimental conditions have been optimized to reduce water evaporation and irradiation damage. The choice of the reconstruction algorithm has been discussed. Moreover, Monte Carlo simulations have shown that the minimum quantity of water which could be detected in tomograms did not depend on the materials composition but could realistically be estimated through Crowther's criterion. The detection of smaller thicknesses of water therefore requires to work on thinner samples and/or to increase the number of projection images, this increase being still limited by irradiation damage. This will imply to reconstruct the volume from a limited number of images and poor signal-to-noise ratios.

The 3D characterization of water-containing samples was possible before using X-ray tomography, with a resolution of about 1 micron. Higher resolutions could be obtained on frozen samples by TEM tomography on cryosections, or by Scanning Transmission X-Ray Microscopy (STXM). Despite irradiation damage, wet-STEM tomography is complementary to those techniques. As far as the resolution is concerned, it is similar to STXM but images with a good contrast can be acquired even on amorphous samples containing only light elements. Its main advantage probably lies in the fact that *in situ* experiments such as hydration / dehydration become possible. For example, it should be able to follow the 3D arrangement of latex particles during filmification, or the fabrication of gypsum or cement-based materials. Because of irradiation damage, the observation of live biological samples

may be more difficult and require further developments to reduce the electron dose received by the sample.

## **Acknowledgements**

The authors acknowledge the Centre Lyonnais de Microscopie (CLYM) for the access to the ESEM XL-30 FEG microscope and the Institut Universitaire de France (IUF) for financial support. The authors would also like to acknowledge M. Michelin-Jamois and P. Perriat for having kindly provided the MCM-41 and gold-polysiloxane samples, respectively, as well as R.F. Septiyanto and F. Iskandar who have been involved in the Monte Carlo simulations. S.B. acknowledges the IAP-PAI interuniversity network supported by the Belgian government and the European Research Council under the 7th Framework Program (FP7), ERC grant N°335078 – COLOURATOMS. KMV dedicates this paper to Agnès Bogner, who was involved in this project.

## **References**

- BLAVETTE, D., BOSTEL, A., SARRAU, J.M., DECONIHOUT, B. & MENAND, A. (1993). An atom probe for three-dimensional tomography. *Nature* **363**, pp. 432-435.
- BOGNER, A., THOLLET, G., BASSET, D., JOUNEAU, P.H. & GAUTHIER, C. (2005). Wet-STEM: a new development in environmental SEM for imaging nano-objects included in a liquid phase. *Ultramicroscopy* **104**, pp. 290-301.
- BOGNER, A. (2006) Le mode d'imagerie wet-STEM : développement, optimisation et compréhension. Application aux mini-émulsions et latex. *PhD thesis*, INSA de Lyon, France. Available online at <http://theses.insa-lyon.fr/publication/2006ISAL0066/these.pdf> (19/09/2013).

- CROWTHER, R.A., DEROSIER, D.J. & KLUG, A. (1970). The reconstruction of a three-dimensional structure from projections and its application to electron microscopy. *Proceedings of the Royal Society A* **317**, pp. 319-340.
- DANILATOS, G.D. (1993). Introduction to the ESEM instrument. *Microscopy Research Technique* **25**, pp. 354-361.
- DE JONGE, N. & ROSS, F.M. (2011). Electron microscopy of specimens in liquid. *Nature Nanotechnology* **6**, pp. 695-704.
- DONALD, A.M. (2003). The use of environmental scanning electron microscopy for imaging wet and insulating materials. *Nature materials* **2**, pp. 511-516.
- FLETCHER, A.L., THIEL, B.L. & DONALD, A.M. (1997). Amplification measurements of alternative imaging gases in environmental SEM. *Journal of Physics D: Applied Physics* **30**, pp. 2249.
- GAUTHIER, C., JORNSANO, P., MASENELLI-VARLOT, K. & THOLLET, G. (2006). Montage pour effectuer de la tomographie électronique dans un microscope électronique à balayage et à pression contrôlée. *FR patent* 06-09-708.
- GORIS, B., VAN DEN BROEK, W., BATENBURG, K.J., HEIDARI MEZERJI, H. & BALS, S. (2012). Electron tomography based on a total variation minimization reconstruction technique. *Ultramicroscopy* **113**, pp. 120-130.
- GORIS, B., ROELANDTS, T., BATENBURG, K.J., HEIDARI MEZERJI, H. & BALS, S. (2013). Advanced reconstruction algorithms for electron tomography: from comparison to combination. *Ultramicroscopy* **127**, pp. 40-47.
- HARAUZ, G. & VAN HEEL, M. (1986). Exact filters for general geometry three dimensional reconstruction. *Optik* **73**, pp.146–156.

HUANG W., YIBEI F., CHAOYANG W., YUNSHU X. & ZHISHANG B. (2002). A study on radiation resistance of siloxane foam containing phenyl. *Radiation Physics and Chemistry* **64**, pp. 229-233.

JORNSANOH, P., THOLLET, G., FERREIRA, J., MASENELLI-VARLOT, K., GAUTHIER, C. & BOGNER, A. (2011). Electron tomography combining ESEM and STEM: a new 3D imaging technique. *Ultramicroscopy* **111**, pp. 1247-1254.

KOSTER, A.J., ZIESE, U., VERKLEIJ, A.J., JANSSEN, A.H. & DE JONG, K.P. (2000). Three-dimensional Transmission Electron Microscopy: a novel imaging and characterization technique with nanometer scale resolution for materials science. *J. Journal of Physical Chemistry B* **104**, pp. 9368-9370.

KUBIS, A.J., SHIFLET, G.J., DUNN, D.N. & HULL, R (2004). Focused ion-Beam Tomography. *Metallurgical and materials Transactions A* **35A**, pp. 1935-1943.

LEARY, R., MIDGLEY, P.A. & THOMAS, J.M. (2012). Recent advances in the application of electron tomography to materials chemistry. *Accounts of Chemical Research* **45**, pp. 1782-1791.

MAIRE, E., BUFFIERE, J.Y., SALVO, L., BLANDIN, J.J., LUDWIG, W. & LETANG, J.M. (2001). On the application of X-ray microtomography in the field of materials science. *Advanced Engineering Materials* **3**, pp. 539-546.

MANCUSO, J.J. (2012) Large volumes at high resolution using serial block face imaging in the SEM. *Microscopy and Microanalysis* **18**, **S2**, pp. 104-105.

MARTINI, M., ROUX, S., MONTAGNA, M., PANSU, R., JULIEN, C., TILLEMENT, O. & PERRIAT, P (2010). How gold inclusions increase the rate of fluorescein energy homotransfer in silica beads. *Chemical Physics Letters* **490**, 72-75.

MESSAOUDI, C., BOUDIER, T., SANCHEZ SORZANO, C.O. & MARCO, S (2007). TomoJ : tomography software for three-dimensional reconstruction in transmission electron microscopy. *BMC Bioinformatics* **8**, pp. 288-297.

MESSAOUDI, C., ASCHMAN, N., CUNHA, M., OIKAWA, T., SANCHEZ SORZANO, C.O. & MARCO, S. (2013). Three dimensional chemical mapping by EFTEM-TomoJ including improvement of SNR by PCA and ART reconstruction of volume by noise suppression. *Microscopy and Microanalysis* **28**, pp 1-9..

NELSON, A.C. (1988). Scanning electron microscope for visualization of wet samples. *US patent* 4,720,633.

PECKYS, D.B. & DE JONGE, N. (2011). Visualization of gold nanoparticle uptake in living cells with liquid scanning transmission electron microscopy. *Nano Letters* **11**, pp. 1733-1738.

RIBEIRO CARROTT M.M.L., Estêvão Candeias, Carrott P.J.M. & Unger, K.K. (1999). Evaluation of the stability of pure silica MCM-41 toward water vapor. *Langmuir* **15**, pp. 8895-8901.

RING, E.A. & DE JONGE, N. (2012). Video-frequency scanning transmission electron microscopy of moving gold nanoparticles in liquid. *Micron* **43**, pp. 1078-1084.

RUSKA, E. (1942). Beitrag zur übermikroskopischen Abbildungen bei Höheren Drucken. *Kolloid-Zeitschrift* **100**, pp. 212-219.

TREWYN, B.G., SLOWING, I., GIRI, S., CHEN, H.T.,& LIN, V.S. (2007). Synthesis and functionalization of a mesoporous silica nanoparticle based on the sol-gel process and applications in controlled release. *Acc Chem Res.* **40**, pp. 846-853.

WEYLAND, M. (2002) Electron tomography of catalysts. *Catalysis* **21**, pp. 175-183.

ZHAO X.S., AUDSLEY, K. & LU, G.Q. (1998). Irreversible change of pore structure of MCM-41 upon hydration at room temperature. *Journal of Physical Chemistry B* **102**, pp. 4143-4146.

## **Table captions**

Table 1 : thicknesses (nm), calculated with Monte Carlo simulations on several materials, required to detect 10, 20, 30 or 50 nm of water. The determination coefficients are calculated when considering linear regressions of the sample thicknesses in function of either their densities or the water thickness. The resolution determined using the Crowther criterion is also reported, with the sample thickness equal to the average value for each water layer thickness. With a level of confidence of 95%, it is found that the maximum sample thickness depends on the water thickness but not on the sample density. For one sample thickness, the values found from the Crowther's criterion are of the same orders of magnitude as the minimum water thicknesses.

## Figure captions

Figure 1: device for wet-STEM tomography in the ESEM, composed of a) a rotation and b) two translation piezoelectric elements; c) a sample holder and d) a STEM detector placed below the sample. The dashed lines represent the position of the Peltier stage.

Figure 2 : geometry used for Monte Carlo simulations. Electron Beam 1 nm; Collection angles between 14 and 40°. The dimensions of the MCM41 box have been chosen to limit the number of electrons escaping the sides of the box.

Figure 3: a) typical image of gold/polysiloxane nanoparticles in suspension in water, at tilt angle equal to 0° (acceleration voltage 30kV, probe size 3; magnification 100,000; H<sub>2</sub>O pressure 5.6 Torr; temperature 2°C; pixel size 0.9 nm); b) TEM bright field image of the nanoparticles, from (Martini et al. 2010); c) 3D view of the reconstructed volume. The gold cores have been segmented and are represented in red. d) Results of the Fourier Shell Correlation analysis. Resolution  $\approx$  1 nm (0.5 threshold), actually limited by the probe size.

Figure 4: raw images obtained on a hydrophilic MCM-41 grain a), b), c) in the dry state (H<sub>2</sub>O pressure 4.5 Torr) and d), e), f) after water condensation (H<sub>2</sub>O pressure 6 Torr). The tilt angles were set to 50° for a) and d), 0° for b) and e) and -50° for c) and f). Acceleration voltage 30kV, probe size 3; magnification 7,500; temperature 2°C; pixel size 13 nm. g) plot profile along the line represented on b) showing a decrease of the contrast inside the MCM41 grain.

Figure 5 : XY, YZ and XZ slices of a tomogram calculated from the projection series presented in Figure 4d, e, and f (tilt range  $\pm$ 50°, tilt step 10°), and using the Algebraic

Reconstruction Technique method (ART) after denoising by the BgART algorithm. Artefacts due to the large tilt step are clearly visible.

Figure 6 : a) and b) segmented reconstructed volume calculated from the projection series presented in Figure 4d, e, and f (tilt range  $\pm 50^\circ$ , tilt step  $10^\circ$ ), and using a Total Variation Minimization algorithm. Tilt angles similar to those of the projection series presented in Figure 4. c) YZ, d) XY and e) XZ orthoslices. The overall shape of the MCM41 grain and the water droplet are resolved in the tomogram.

Figure 7 : number of collected electrons for several MCM-41 and water layer thicknesses. The number of collected electrons slightly increases for MCM41 thicknesses smaller than  $1 \mu\text{m}$ .

Figure 8 : variations of the contrast observed between the dry and the wet states, for several MCM-41 and water layer thicknesses. When arbitrarily setting a contrast detection limit greater than or equal to 5%, a maximum MCM-41 thickness can be defined for each water layer thickness.

Materials	Density (g/cm <sup>3</sup> )	10 nm H <sub>2</sub> O	20 nm H <sub>2</sub> O	30 nm H <sub>2</sub> O	50 nm H <sub>2</sub> O	DETERMINATION COEFFICIENTS
MCM-41	0.9	50	150	200	500	0.9657
SBA-15	1.19	240	-	230	230	0.75
Carbon	2.27	150	200	240	230	0.6349
Silica	2.65	220	290	340	400	0.9668
CaCO <sub>3</sub>	2.71	220	290	320	330	0.7475
TiO <sub>2</sub>	3.95	220	290	340	400	0.9568
Al <sub>2</sub> O <sub>3</sub>	4.23	220	250	260	260	0.6385
DETERMINATION COEFFICIENTS		0.2916	0.5099	0.4058	0.0279	
AVERAGE VALUES (nm)		189	245	276	336	
CROWTHER RESOLUTION (nm)		33	43	48	59	

Table 1

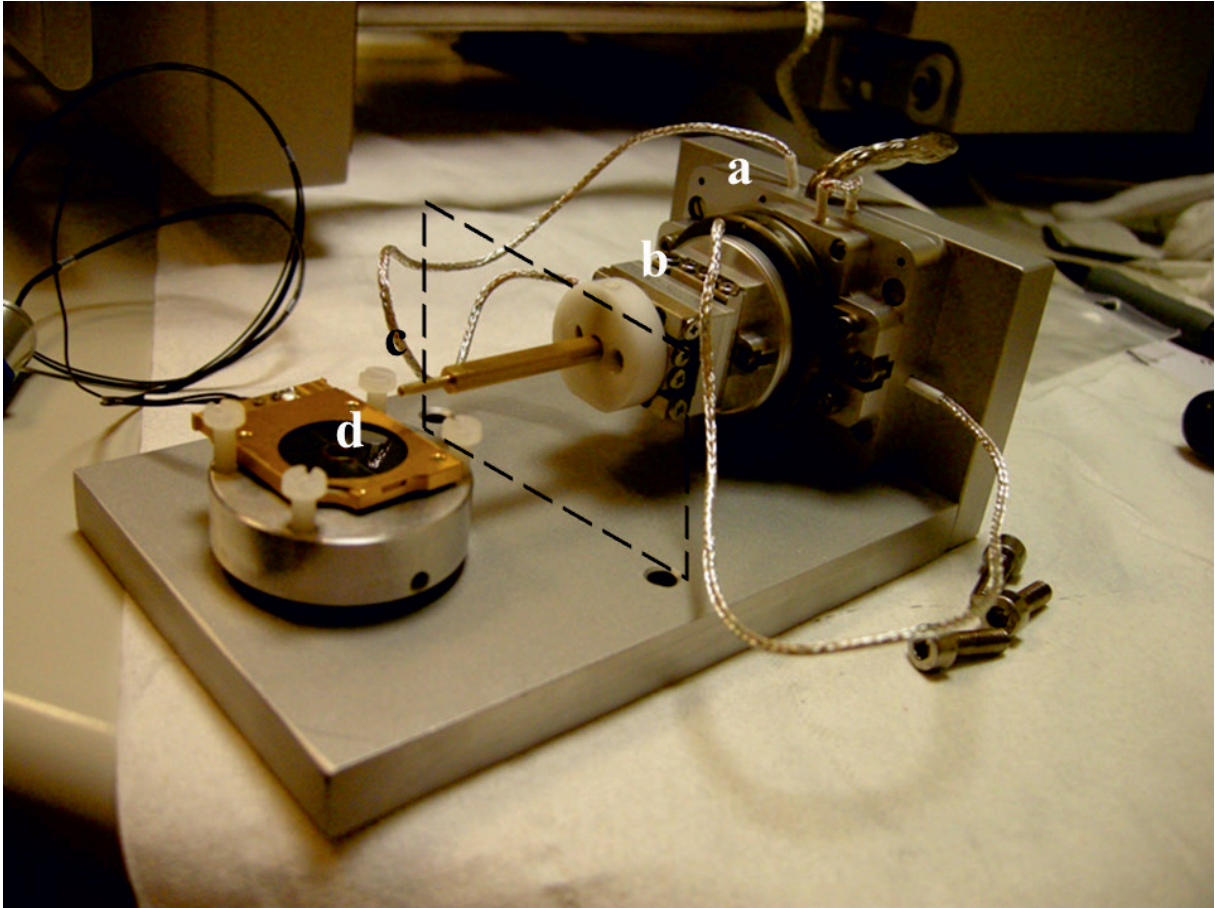


Figure 1

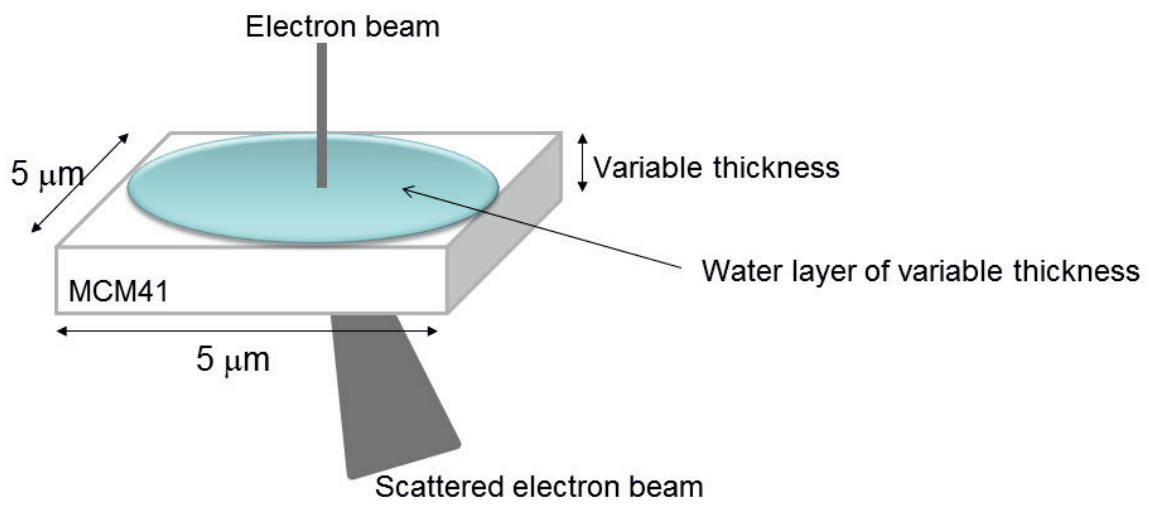


Figure 2

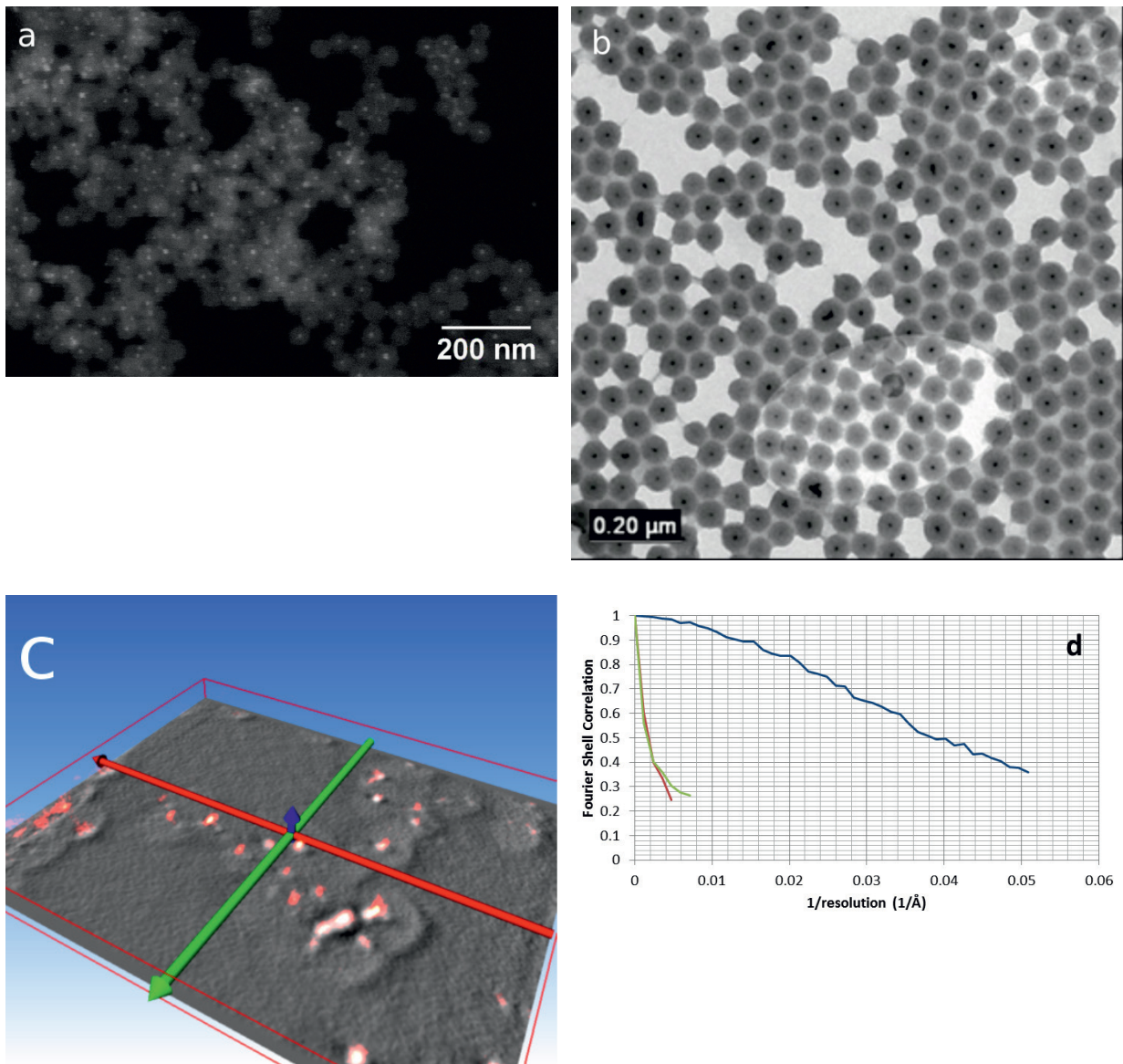
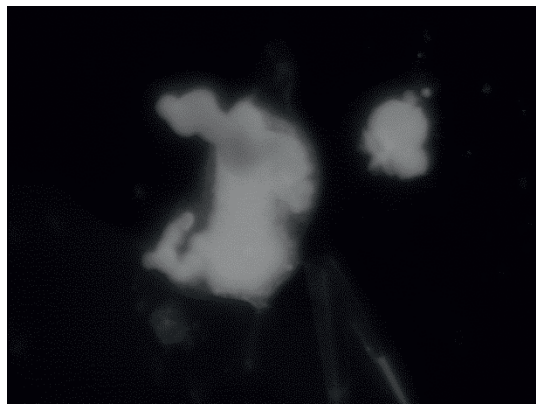
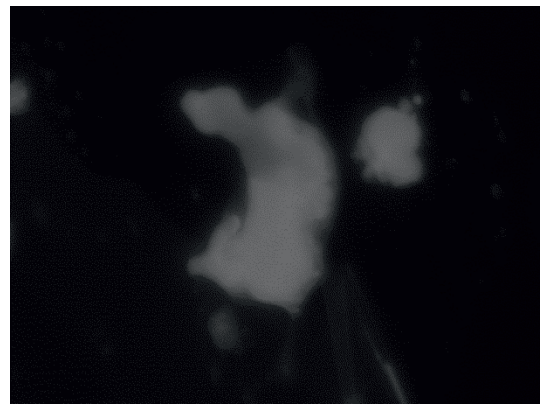


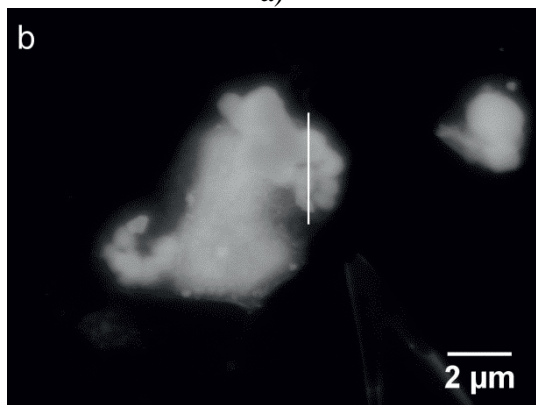
Figure 3



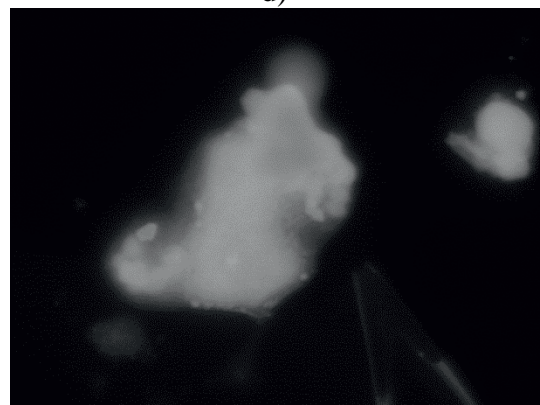
a)



d)



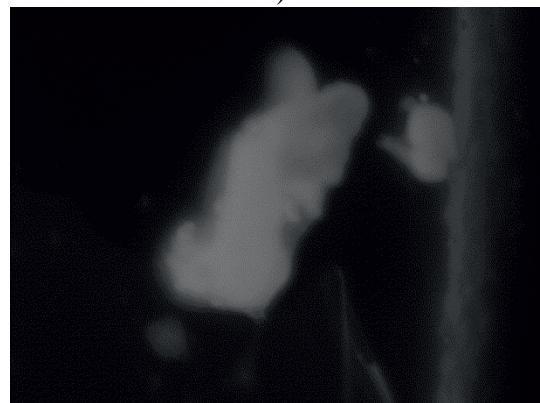
b)



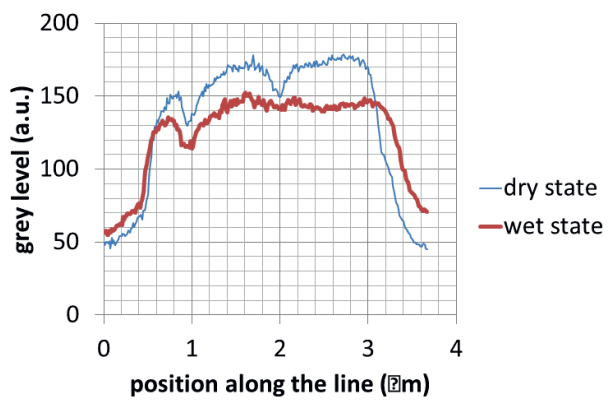
e)



c)



f)



g)

Figure 4

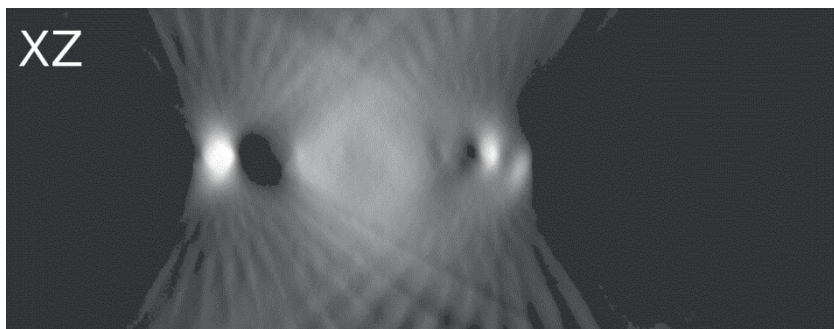
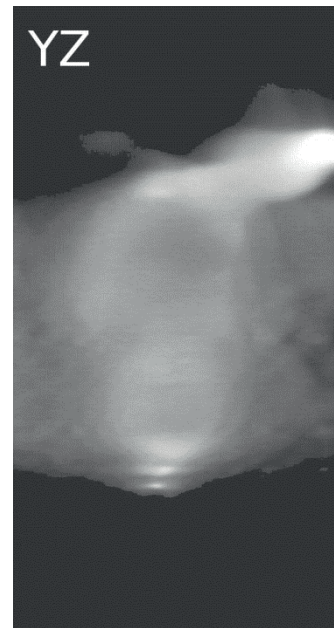
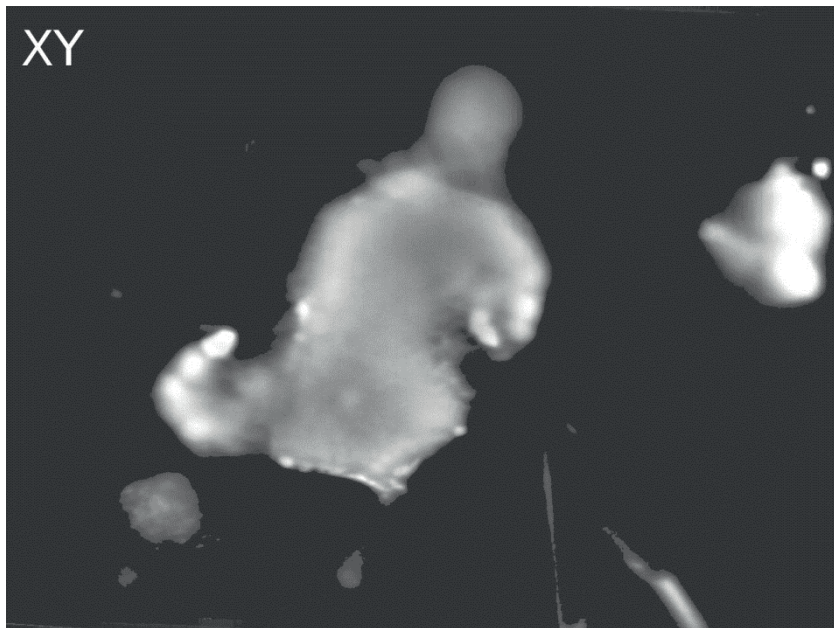


Figure 5

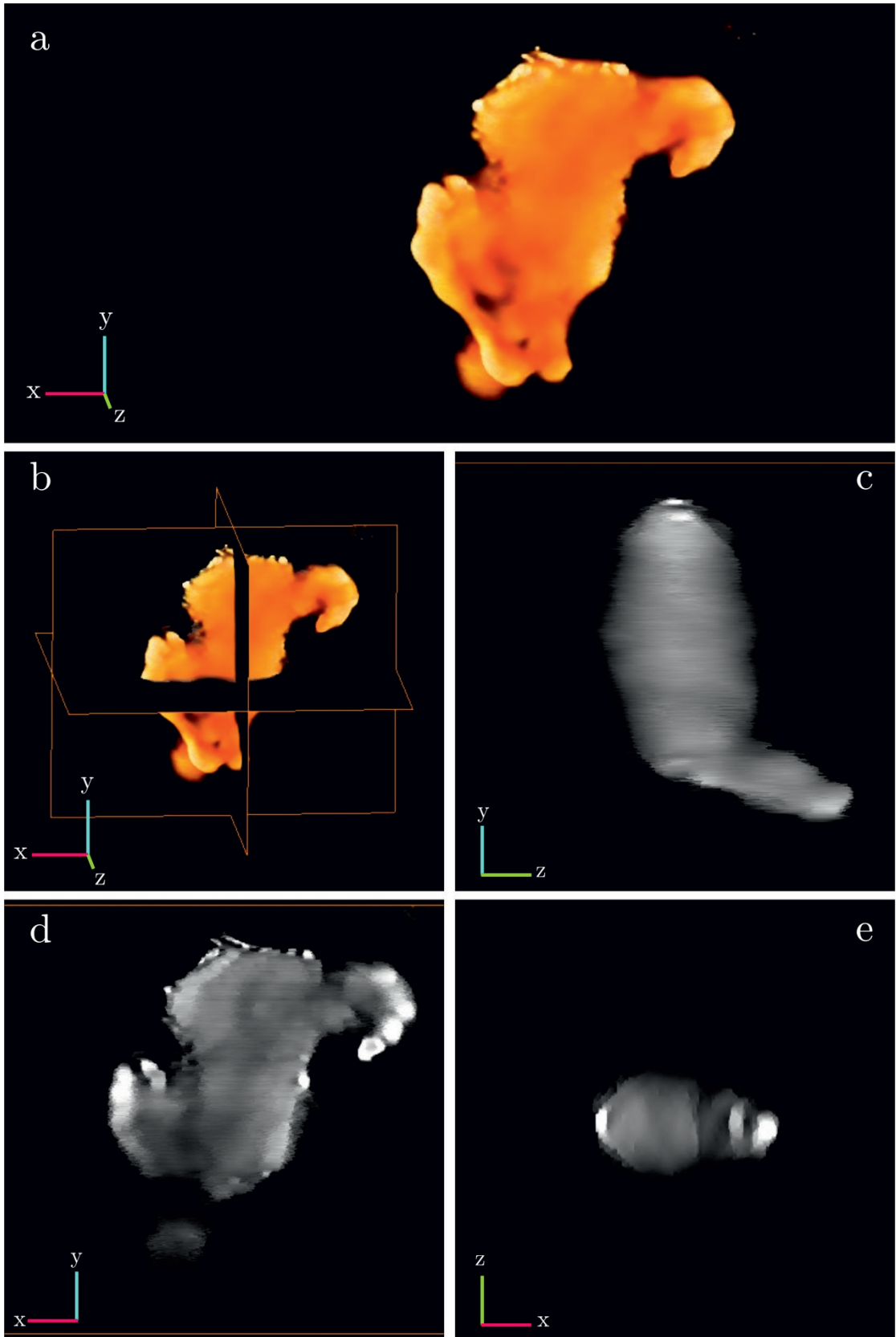
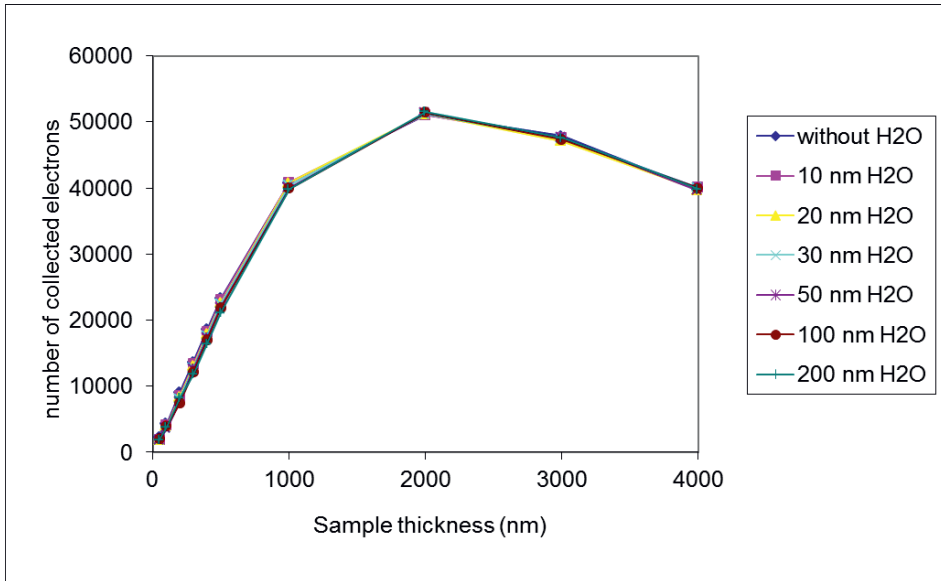
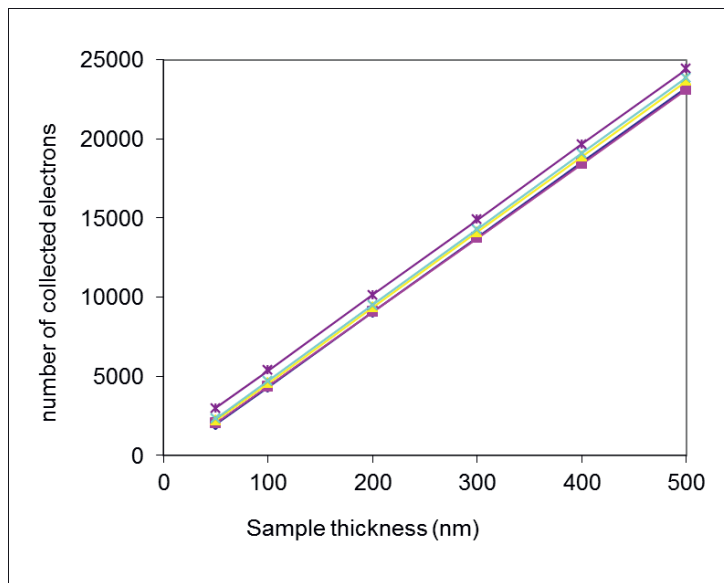


Figure 6



a)



b)

Figure 7

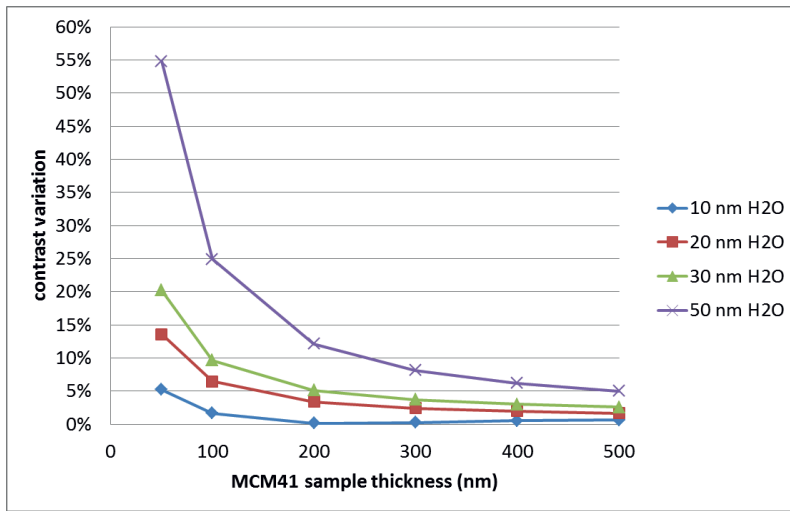


Figure 8